Research Article Vol. 58, No. 33 / 20 November 2019 / Applied Optics 9267

applied optics

Experimental studies of the transmission of light through low-coverage regular or random arrays of silica micropillars supported by a glass substrate

Colette Turbil,[1] Thomas Sang Hyuk Yoo,[2] Ingve Simonsen,[1,3] Jeremie Teisseire,[1] Iryna Gozhyk,[1,*] and Enric Garcia-Caurel[2]

[1]SVI, UMR 125 CNRS/Saint-Gobain Recherche, 39 quai Lucien Lefranc, 93303 Aubervilliers, France
[2]LPICM, CNRS, Ecole Polytechnique, Université Paris-Saclay, 91128 Palaiseau, France
[3]Department of Physics, NTNU—Norwegian University of Science and Technology, NO-7491 Trondheim, Norway
*Corresponding author: iryna.gozhyk@saint-gobain.com

Received 30 August 2019; revised 17 October 2019; accepted 19 October 2019; posted 21 October 2019 (Doc. ID 376740); published 20 November 2019

The transmission of light through low-coverage regular and random arrays of glass-supported silica micropillars of diameters 10–40 μm and height 10 μm is studied experimentally. Angle-resolved measurements of the transmitted intensity are performed at visible wavelengths by either a goniospectrophotometer or a multimodal imaging (Mueller) polarimetric microscope. It is demonstrated that for the regular arrays, the angle-resolved measurements are capable of resolving many of the densely packed diffraction orders that are expected for periodic structures of lattice constants 20–80 μm, but they also display features ("halos" and fringes) that are due to the scattering and guiding of light in individual micropillars or in the supporting glass slides. These latter features are also found in angle-resolved measurements on random arrays of micropillars of the same surface coverage. Finally, we perform a comparison of direct measurements of haze in transmission for our patterned glass samples with what can be calculated from the angle-resolved transmitted intensity measurements. Good agreement between the two types of results is found, which testifies to the accuracy of the angle-resolved measurements that we report.

https://doi.org/10.1364/AO.58.009267

1. INTRODUCTION

Surfaces with features from macro- [1] to nanoscale [2] can be found in both nature and industrial products. Such features cause light scattering and diffraction, and therefore, they impact the visual appearance of objects. Among the phenomena related to light scattering and diffraction, there are many non-exotic effects that can be experienced in everyday life: reflection of light from, or transmission trough, a rough surface [3,4]; diffraction through apertures [5] (holes in the window blinds) or from or through a transparent/opaque material of a particular shape (Mie scattering [6]); and diffraction from periodic structures (diffraction grating [7] and photonic crystals [8]). In textbooks, these phenomena are often considered a separate phenomenon and often restricted to a particular range of parameters. For instance, "diffraction grating" analysis is almost exclusively applied to periodic structures for which the lattice constants are comparable to the wavelength of the incident light, which for visible light, corresponds to roughly 0.5–2 μm. Meanwhile, the habit of considering only specific cases of light scattering and diffraction for a particular range of parameters may lead to an incorrect approach to the characterization of samples and thus to inaccurate or even incorrect interpretation of experimental data.

Nowadays, micro- and nano-fabrication techniques allow for surface and volume modification at a scale down to sub-micrometer and over macroscopic dimensions [9]. Periodic patterns with lattice constants from tens to hundreds of micrometers exhibit hundreds to thousands of (propagating) diffraction orders when the sample is illuminated by visible light. Although such structures are by no means efficient diffraction gratings, they can still produce a noticeable effect on the optical properties of the samples and thus their visual appearances, as will be shown in this paper. Meanwhile, numerical analysis of their optical properties is computationally very demanding, since the ratios of lattice constants to wavelength typically can reach $10^1 - 10^2$. Thorough experimental analysis appears to be the only reasonable approach in studying such systems. Moreover, if several feeble optical effects are brought together, they can impact significantly the optical response of

the surfaces, while it remains difficult to predict such different features with a single simulation tool.

Measurements of gloss and haze are often the first step in the experimental characterization of the optical properties of samples that scatter light due to surface patterns or volume disorder. The simple integral optical properties—haze and gloss—allow a distinction of the light that is reflected/transmitted specularly by the sample from the light that is scattered diffusely by it. However, the actual spectral and angular distributions of the intensity of the scattered light can be rather complex. Despite the convenience of haze and gloss in terms of measurement ease and speed, such integral properties may misguide the interpretation, which is a big issue for quality control, especially if such measurements contain artifacts related to the diffraction of light. Finally, it is important to identify various non-classic angle-resolved optical properties that can be provided by surface patterning and are likely to be distinguishable by a human eye, to account for such features in bidirectional reflectance or transmittance distribution functions (BRDF and BTDF), which are the basis of the virtual reality rendering tools.

The rest of this paper is organized in the following way. Section 2 presents the samples that we will study in this work and the instruments used to perform the angle-resolved intensity measurements. Such and other results are presented in Section 3, where we also discuss and interpret the various features that are present in them. In particular, in this section, we discuss the origin of the different types of circular intensity fringes that the angle-resolved transmitted intensity distributions possess. The haze of the samples, both directly measured and obtained on the basis of the angle-resolved measurements, is also discussed here [Section 3.B]. Finally, the conclusions that can be drawn from this work are presented in Section 4.

2. MATERIALS AND METHODS

A. Description of the Samples

Surfaces patterned with micro-pillars have been studied since the early 2000s as model surfaces for hydrophobicity [10–12]. The studied samples consisted of 5×5 cm^2 glass slides covered by an array of cylindrical silica micropillars [Fig. 1]; all cylinders had the height $h = 10$ μm, while their diameters were $d = 10$ μm, 20 μm, or 40 μm. Both regular and random arrays were studied. The regular arrays were either hexagonal or square, for which the lattice vectors were $\mathbf{a}_1 = a\hat{\mathbf{x}}$ [both cases] and $\mathbf{a}_2 = (a/2)[-\hat{\mathbf{x}} + \sqrt{3}\hat{\mathbf{y}}]$ [hexagonal] or $\mathbf{a}_2 = a\hat{\mathbf{y}}$ [square], where $\hat{\mathbf{x}}$ and $\hat{\mathbf{y}}$ are orthogonal unit vectors in the sample plane (the xy plane). The lattice constant a of the regular arrays varied from 20 μm to 80 μm [Fig. 1]. The surface coverage ρ is defined as the ratio between the areas of the base of one micropillar to the area of a unit cell. For a hexagonal array, one finds $\rho = (\pi/2\sqrt{3})(d/a)^2$, while for a square array, $\rho = (\pi/4)(d/a)^2$ [13]. For instance, pillars of diameter 10 μm arranged in a hexagonal array and with a lattice constant in the previously given range of values correspond to a surface coverage between $\rho = 1.4\%$ ($a = 80$ μm) and 22.7% ($a = 20$ μm). Random arrays were produced to have the same surface coverage as the regular arrays for the same type of micropillars. To this end, the centers of the pillars were chosen to be uniformly distributed in such a way that two pillars could not be closer to each other than a minimum center-to-center distance (20 μm). About a 300 nm thick residual silica layer between the glass surface and the base of the pillars provided an adhesion layer for the pillars to the surface of the substrate [Fig. 1]. The thickness of the glass substrates was 2 mm for the majority of samples, and 1 mm for samples measured with the multimodal microscope. All the samples were produced in solgel silica by use of the nanoimprinting technique (for a detailed description, see Ref. [12]). If necessary, the refractive index of the solgel layer prior to patterning can be adapted through doping of solgel solution or modifying the solgel matrix [14].

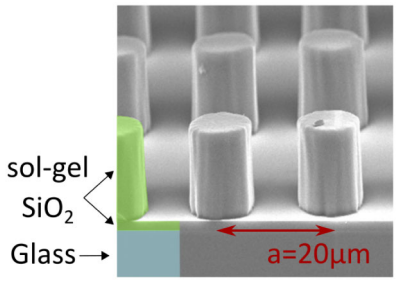

Fig. 1. Scanning electron microscope image of a cross section of the sample taken at grazing incidence. The height of all micropillars used in this study is $h = 10$ μm.

B. Optical Measurements

Conventional integral haze and gloss measurements were used in this study together with two facilities for angle-resolved measurements: OMS4 goniospectrophotometer (commercialized by OPTIS) and a homemade multimodal imaging (Mueller) polarimetric microscope. Both angle-resolved setups allow for the measurements of the optical intensity response of the sample. Since the two instruments are based on very different optical configurations, we decided to use them both to verify the consistency of the results and to identify the presence of possible artifacts due to the instrument response functions. Despite the fact that the two instruments also allowed for the measurement of the state of polarization of the transmitted or reflected light [15], this paper focuses on the angular distribution in the far field of the intensity transmitted through the sample regardless of its polarization.

The integral optical properties, haze and gloss, were obtained by use of a *hazemeter* (BYK Gardner Haze-gard plus) for measurements in transmission and a *glossmeter* (Enrichsen–Pico Glossemaster Model 500) for measurements in reflection.

As a goniospectrophotometer device, OMS4 consists of the sample holder and two arms, where one of the arms has a set of light sources installed and the other a photomultiplicator detector. The sample holder and the detector arm can be moved automatically with the help of one and two precise motors, respectively. This allows to scan the whole angular region around the sample and thus to measure the angular intensity distributions of the reflected or transmitted light, at any angle of incidence in the range of $\theta_i \in [0°, 85°]$.

In this study, OMS4 was used in transmission mode to measure the angular distribution of the transmitted intensity; the angular resolution was 0.5° around the specular direction.

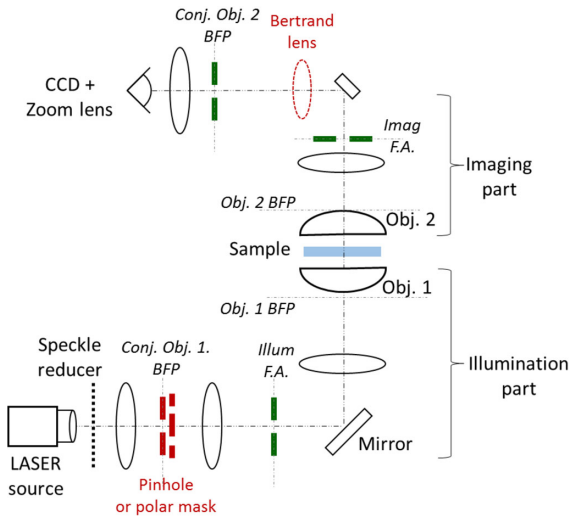

Fig. 2. Schematic illustration of the multimodal (Mueller) microscope in the transmission configuration. The positions of the conjugate images corresponding to the back-focal planes (BFP) of the two objectives, as well as the conjugate planes of the sample in the illumination and imaging arm are shown. Also indicated are the positions of the retractable Bertrand lens, the light source, and the detection camera.

Measurements were performed with three coherent laser sources (RGB) and an incoherent Xenon lamp light with or without color filters. The BTDF [16] of the samples was collected for the polar angles of incidence $\theta_i = 0°$, 10°, 30°, and 60°. A related function, the differential transmission coefficient (DTC) [17], is obtained by multiplying the BTDF by the cosine of the polar angle of transmission $[\cos\theta_t]$. The contour plots of the DTC, obtained in this way from the data measured by OMS4, were plotted with the SPEOS software package produced by OPTIS.

The main difference between the goniospectrophotometer and the multimodal polarimetric microscope is the absence of moving parts in the latter system. The multimodal microscope can be operated in two imaging modes, real plane and Fourier (or conjugate space) plane imaging modes. In real plane imaging mode, the microscope produces images of the studied sample, while in Fourier imaging mode, the images correspond to the angular distribution of light transmitted or reflected by the sample. The optical configuration of the multimodal microscope is sketched in Fig. 2. The instrument was coupled to a laser emitting green light at a wavelength of 533 nm with a spectral width of less than 2 nm. Speckle effects due to the coherence of the laser were minimized using a vibrating rough membrane (Laser Speckle Reducer from Optotune) just in front of the laser source. The microscope was mounted in the transmission configuration; the sample was located between two identical microscope objectives (one for imaging and another one for illumination). The microscope objectives can be selected to have different magnifications, 50×, 20×, 10×, or 5×, depending on the required resolution and a numerical aperture.

Due to the use of a series of relay lenses, it is possible to create conjugate images of the back-focal planes (BFP) of the objectives in both the illumination and imaging parts. Therefore, we can insert apertures in the conjugate plane of the BFP of the illuminating objective with different shapes and sizes to simultaneously control the direction and the angular aperture of the illuminating beam. Analogously, the insertion of a pinhole or polar mask at the conjugate plane of the BFP of the imaging microscope objective, allows controlling the direction and aperture of the detected scattered beam.

The direction of the illuminating beam is defined by the mean polar angle of incidence $\langle\theta_i\rangle = \arcsin(D/f)$. Here, f is the focal length of the microscope objective and D the off-axis distance measured from the center of the pinhole to the optical axis of the microscope. For instance, if a pinhole is placed in the plane conjugated to the illuminating objective BFP, and this same pinhole is shifted to a given distance to the optical axis, then the sample can be illuminated with an oblique incidence. When the pinhole is aligned with the microscope optical axis, the sample is illuminated at normal incidence.

Moreover, once the average polar angle $\langle\theta_i\rangle$ is known, the divergence (div in radians) of the illumination, or alternatively, the imaging beam, can be expressed as a function of the corresponding pinhole diameter ϕ_{pin}, the focal length of the microscope objective f, and the mean polar angle according to

$$\text{div} = \frac{\phi_{\text{pin}}}{f\cos\langle\theta_i\rangle}. \tag{1}$$

The relay lens system also provides a conjugate of the object plane (the sample) in both the illumination and the imaging arms; therefore, the use of pinholes or polar masks in those planes helps to define the shape and size of the illuminated and imaged areas of the sample, or, in other words, the field of view (FOV). The insertion of a Bertrand lens in the optical path of the microscope allows to easily switch between the real and the Fourier imaging modes [18]. In summary, the measurements performed with the homemade multimodal imaging (Mueller) polarimetric microscope are much faster than those performed with the goniospectrophotometer. The polarimetric microscope also allows for measurements in both the Fourier and real plane imaging modes, and the aperture of its illumination can be controlled in a precise manner. On the other hand, the goniospectrophotometer has higher angular resolution (down to 0.1° for measurements using a laser), better dynamic range (up to 8 decades), and larger angular range for angles of incidence and detection.

3. RESULTS AND DISCUSSION

First, in this section, we are concerned with the angle-resolved measurements for both the regular and the random arrays of micropillars and the discussion of the features that such data show. Later, we address the integral optical properties of the samples, such as haze and gloss. This will be done by direct measurements of haze, but also by calculations based on the angle-resolved measurements that we performed.

A. Angle-Resolved Measurements

In standard scatterometry measurements, such as BTDF or DTC measurements, the direction of illumination and detection are both selected by moving the goniometric arms on which the source and the detector are mounted, respectively. In the multimodal microscope, however, the control of the direction

of the beam in both the illumination and the imaging arm is obtained by the use of pinholes placed at different positions in the conjugate planes (BFP) of the microscope objective, as previously discussed. These intrinsic differences in how the measurements are performed with these two setups make a comparison of the obtained data very interesting.

Figure 3 presents contour plots of the angular distribution of the normalized DTCs obtained for a sample of a hexagonal array of micropillars and measured by either the goniospectrophotometer [Figs. 3(a)–3(b)] or the microscope [Fig. 3(c)]. The normalization was done with respect to the maximum value of the angular-dependent DTC, which in our case, was found in the direction of specular transmission.

We first start by discussing the measurements performed with the goniospectrophotometer. In the outer brown region in Figs. 3(a) and 3(b), no measurements were performed, since either the detector arm covered the source [around $\phi_t = 0°$] or the angular region was inaccessible to the detector due to the physical dimensions of the support on which the setup was mounted [around $\phi_t = 270°$]. The specular direction of transmission in Fig. 3, and in the preceding experimental results to be presented, is at $(\theta_t, \phi_t) = (\theta_i, \phi_i - 180°) = (\theta_i, 0°)$. The sample consisted of cylindrical pillars of diameter $d = 10$ μm, and the lattice constant was $a = 30$ μm [$\rho = 10\%$]. The angles of incidence assumed in obtaining the results in Fig. 3(a) are $(\theta_i, \phi_i) = (0°, 180°)$ while in Figs. 3(b)–3(c), the angles of incidence are $(\theta_i, \phi_i) = (30°, 180°)$. In obtaining the results in Figs. 3(a)–3(b), the illuminating source consisted of a Xenon lamp to which a 10 nm wide spectral filter centered at 535 nm was applied; a laser source of wavelength $\lambda = 533$ nm was used to obtain the results presented in Fig. 3(c). All the transmitted light, independent of polarization, was detected. It is challenging to accurately align the micro-patterned sample in the macroscopic setup, so therefore, the azimuthal angle of incidence may show slight deviations from $\phi_i = 180°$. It should be mentioned that for the case of regular arrays of micropillars, for all experiments, we tried to align the samples so that the plane of incidence contained the lattice vector $\mathbf{a}_1$.

Several interesting features should be observed from the results presented in Fig. 3. First, specular peaks of high transmitted intensity are observed in the measurements at $(\theta_t, \phi_t) = (\theta_i, 0°)$, and the transmitted intensities drop off away from this direction.

Second, the measurements have sufficient angular resolution to allow for the observation of the dense pattern of propagating diffractive orders; this is most apparent from the insets in Figs. 3(a) and 3(b). The positions of the propagating diffractive orders are determined by the grating equation and marked by black crosses in the inset in Fig. 3(a). This equation states that the lateral wavevector of transmission is given by

$$\mathbf{q}_{\parallel}^{(m)} = \mathbf{k}_{\parallel} + \mathbf{G}_m, \tag{2}$$

where $\mathbf{G}_m = m_1\mathbf{b}_1 + m_2\mathbf{b}_2$ is a vector defined in terms of the primitive lattice vectors $\mathbf{b}_i$ of the reciprocal lattice, and $m = \{m_1, m_2\}$ denotes a set of two integers [$m_i \in \mathbb{Z}$] defining a diffractive order. The primitive lattice vectors $\mathbf{b}_j$ are obtained from the relations $\mathbf{a}_i \cdot \mathbf{b}_j = 2\pi\delta_{ij}$. For a hexagonal array of lattice vectors $\mathbf{a}_i$ defined in Section 2.A, we obtain

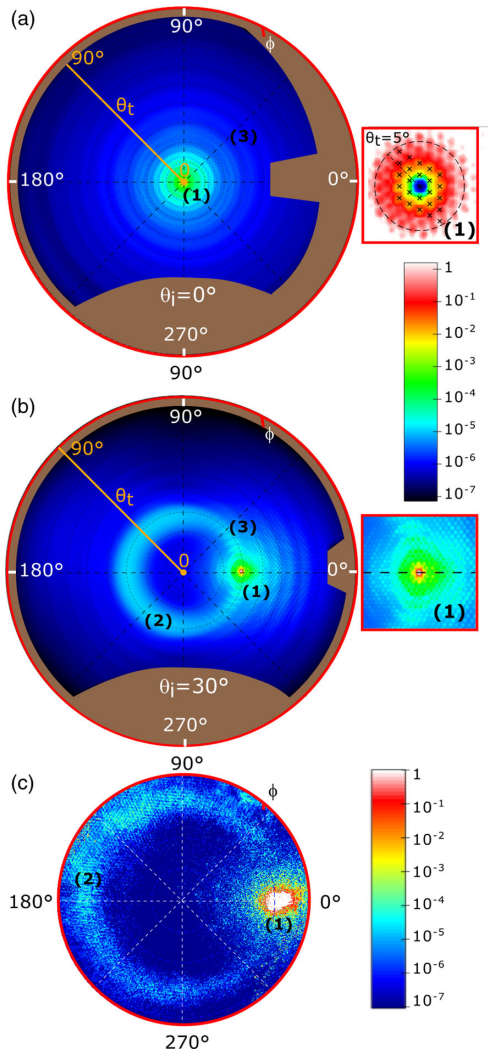

Fig. 3. Angular distribution of the DTCs, normalized by their maximum values and measured with (a)–(b) a goniospectrophotometer and (c) a multimodal microscope in the Fourier plane imaging mode. The polar angle of incidence is (a) $\theta_i = 0°$ and (b)–(c) $\theta_i = 30°$, while the sample consists of a hexagonal array of cylindrical micropillars of diameter $d = 10$ μm, height $h = 10$ μm, and the lattice constant is $a = 30$ μm. The measurements were performed at wavelengths (a)–(b) 535 nm and (c) 533 nm. The brown areas in the top two panels indicate angular region for which measurements could not be performed; see the main text for an explanation. In panel (c), the angular aperture of the illuminating beam is 10°. The angular distribution of the measured DTCs contains three main features (as marked in each of the panels): (1) a specular peak and diffraction orders; (2) a diffuse ring—the "halo"; and (3) concentric patterns. The insets in panels (a) and (b) show the intensity distribution around the specular direction for an angular region of width ±5° (dashed circle) and ±20°, respectively. For better visibility, the color scale of the inset in panel (a) is inverted. Furthermore, we have superposed on it black crosses to indicate the angular positions of a number of diffractive orders calculated on the basis of the grating equation, Eq. (2). The regions of polar angles of transmission over which the measurements were performed are $\theta_t \leq 85°$ [Figs. 3(a)–3(b)] and $\theta_t \leq 45°$ [Fig. 3(c)].

the primitive lattice vectors $\mathbf{b}_1 = (2\pi/a)[\hat{\mathbf{x}} + \hat{\mathbf{y}}/\sqrt{3}]$ and $\mathbf{b}_2 = (2\pi/a)[2\hat{\mathbf{y}}/\sqrt{3}]$. The wavevector $\mathbf{q}_{\parallel}^{(m)}$ of the diffractive order characterized by m and the angles $(\theta_t^{(m)}, \phi_t^{(m)})$

is defined in terms of the angles of transmission as $\mathbf{q}_{\parallel} = (\omega/c)\sin\theta_t(\cos\phi_t, \sin\phi_t, 0)$, with $(\theta_t, \phi_t) = (\theta_t^{(m)}, \phi_t^{(m)})$ where $\omega/c = 2\pi/\lambda$ is the vacuum wave number. The wavevector $\mathbf{k}_{\parallel}$ of the incident light is defined in a similar manner but in terms of the angles of incidence $(\theta_i, \phi_i - 180°)$. The polar angles of transmission $\theta_t^{(m)}$ for the diffractive order characterized by m are therefore obtained from the relation $q_{\parallel}^{(m)} = (\omega/c)\sin\theta_t^{(m)}$ and the corresponding azimuthal angle of transmission from the orientation of the unit vector $\hat{\mathbf{q}}_{\parallel}^{(m)}$. In this way, we calculated the angular positions of the various diffractive orders indicated in the inset in Fig. 3(a) as black crosses; this figure displays a good agreement between the measured and theoretically predicted angular positions of the diffractive orders.

Third, and probably most unexpected and interesting, are the additional complex angular patterns that are visible in the DTC for non-normal incidence [Figs. 3(b)–3(c)] and that are farther away from the specular directions. These features are marked (2) and (3) in Fig. 3(b). The first of these features refers to the *circular structure* of high transmitted intensity seen in this figure. In the following, we will simply refer to it as a "halo." The circular halo is centered at the direction of normal transmission [$\theta_t = 0°$], and it contains the direction of specular transmission $(\theta_t, \phi_t) = (\theta_i, 0°)$. This means that the angular position of the halo is defined by the equation $\theta_t = \theta_i$ (which is also the angular radius of the circular structure). This has the consequence that the halo is predicted to disappear, or coincide with the specular, for light that is incident normally onto the micropillar array. That this is indeed the case can be observed in Fig. 3(a), where the measured data do not show any apparent signs of a halo. The physical origin of the halo feature will be discussed in Section 3.A.2.

The features marked (3) in Fig. 3(b) refer to the "intensity oscillations," or *fringes*, observed in the angular distribution of the DTC in the angular region around the specular direction that also is outside the halo. As will be discussed in greater detail in Section 3.A.3, these fringes belong to two distinct classes of *concentric patterns*: (i) those patterns that are concentric to the normal direction of transmission $(\theta_t, \phi_t) = (0°, 0°)$ [the "origin"] and (ii) those circular fringes that are concentric to the specular direction of transmission. The latter class of fringes is, for instance, readily observed within a 10° cone around the specular direction of transmission in Figs. 3(a)–3(b), while the former class is particularly visible for larger polar angles of transmission Fig. 3(a).

We now turn to the measurement performed by the multimodal microscope. Figure 3(c) presents the result for the angular distribution of the normalized DTC obtained in this way when light was incident at the polar angle of incidence $\theta_i = 30°$ on a hexagonal array of micropillars of the same kind as used to produce the results in Figs. 3(a)–3(b). The microscope measurement was performed for the range of polar angles of transmission $\theta_t \leq 45°$ and all azimuthal angles of transmission ϕ_t with no aperture restriction imposed on the imaging arm. Moreover, the wavelength of the incident light was $\lambda = 533$ nm. This is 2 nm less than the wavelength used to perform the measurements with the goniospectrophotometer, but we believe that this minor difference in wavelength will not cause any significant difference in the obtained results. The four concentric dashed circles seen in Fig. 3(c) indicate the polar angles of transmission $\theta_t = 10°, 20°, 30°$, and 40° (from inner to outer). The white circular area in this figure represents the region around the specular direction.

The angular aperture, Θ, or in other words, the maximum polar angle that can be measured by the multimodal microscope is $\sim 45°$. This value is given by the numerical aperture (NA) of the objective of the microscope used, which in our case was identical to the magnification 50× and an NA of 0.85. In this case, the minimum available thickness of the glass substrate on which the cylinders were deposited was 1 mm. In consequence, using objectives with higher NA and thereby working distance much smaller than 1 mm was not possible in this study.

The angular dependence of the normalized DTC measured with the multimodal microscope is, for the same angles of incidence, similar to the same quantity measured with the goniospectrophotometer. An additional analogy between the images taken with the goniospectrophotometer and the multimodal microscope is the fact that the diffracted orders are also visible in the image taken with the multimodal microscope as an ensemble of regularly spaced spots (light blue) clearly seen on a dark blue background. In the image taken with the goniospectrophotometer, the intensity oscillations due to scattering are easily seen to be located for polar angles of transmission $\theta_t > \theta_i$ (on the right of the specular spot). Unfortunately, in the image taken by the multimodal microscope, this angular region of high contrast falls outside the measured area because the polar angle of the incident beam is close to the maximum aperture accepted by the microscope objective used for the measurements.

1. Diffraction Orders Due to the Regular Array of Pillars

Now we will inspect more closely the intensities and positions of some of the propagating diffractive orders that the hexagonal arrays of micropillars give rise to. Such results will in part provide information on the quality and consistency of the measurements. The results reported in Fig. 3 were obtained using narrowband sources. Therefore, to facilitate a more direct comparison of the measured results to those predicted from the grating equation, Eq. (2), and to study the dependence on the wavelength of the incident light, we performed measurements in the plane of incidence by the use of a laser source of wavelength λ in vacuum. Figure 4(a) presents the dependence of the out-of-plane transmitted intensity measured with the goniospectrophotometer for hexagonal arrays defined by three values of the lattice constant a for normal incidence $[(\theta_i, \phi_i) = (0°, 0°)]$ and wavelength $\lambda = 513$ nm. The angular positions of the diffractive peaks are in good agreement with the predictions from the grating Eq. (2) indicated by the black vertical dashed lines (for $m = \{0, m_2\}$, with $m_2 = 0, \pm 1$) in the figure. Furthermore, the gray shaded region represents the $\theta_t \leq 2.5°$ used in the definition of haze. Good agreement is also obtained between the measured data for $a = 30$ μm and the result obtained from standard diffraction theory when the polar angle of incidence is changed [Fig. 4(b)] or wavelength of the incident light is changed [Fig. 4(c)]. The latter results presented in these figures as black dashed lines are obtained on the basis of Eq. (2). Based on the results in Fig. 4 [and Fig. 3(a)],

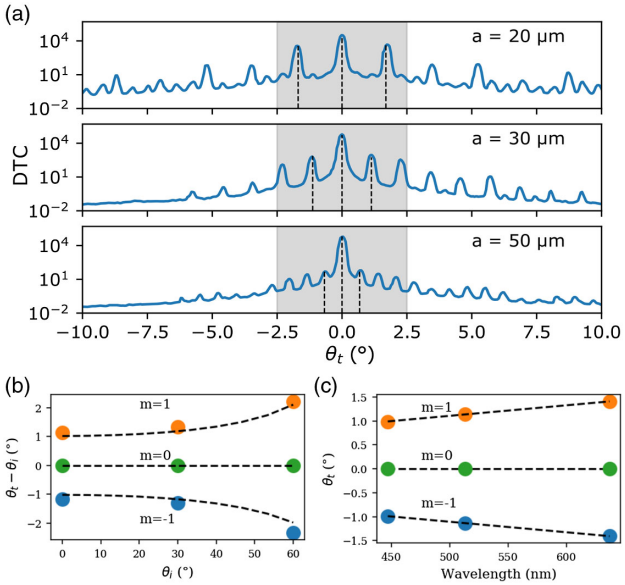

Fig. 4. Out-of-plane dependence of the DTCs measured by the goniospectrophotometer for hexagonal arrays of micropillars ($d = 10$ μm) illuminated by a laser source of wavelength λ. (a) Angular dependence of the out-of-plane DTCs for a set of three values of the lattice constants a for $\theta_i = 0°$ and $\lambda = 513$ nm; the dependence of the polar angle of transmission $\theta_t^{(m)}$ for $m = \{0, m_2\}$ (out-of-plane) obtained experimentally (filled symbols) as a function of (b) polar angle of incidence θ_i for $\lambda = 513$ nm or (c) wavelength λ for normal incidence [$\theta_i = 0°$]. In panels (b) and (c), the lattice constants are, respectively, $a = 30$ μm and $m_2 = 0, \pm 1$. The plane of incidence was chosen so that the lattice vector $\mathbf{a}_1$ lies in this plane. The dashed black lines represent the theoretic values for the polar angle of diffraction $\theta_t^{(m)}$ obtained on the basis of Eq. (2). The shaded gray areas in panel (a) represent the regions for which $\theta_t \leq 2.5°$.

we conclude that our angular-dependent measurements are able to resolve well the densely packed diffractive orders that the regular arrays give rise to; at least this was the case for the values of the lattice constant $a \leq 80$ μm that we considered.

2. *Diffuse Ring or Halo: Impact of the Polar Angle of Incidence*

Next we turn to a discussion of the physical origin and the properties of the halo that is so distinctly present in Fig. 3(b). To this end, we first investigate whether the halo is exclusive to the regular arrays of micropillars or if it also is present in the light transmitted through random arrays of micropillars of similar surface densities. Second, we study how the intensity at the position of the halo $\theta_t = \theta_i$ varies with azimuthal angle when we change the polar angle of incidence θ_i. Figure 5 presents contour plots for the angular distribution of the DTCs, measured with the goniospectrophotometer, and normalized by their maximum values for a set of polar angles of incidence. The samples were patterned by either a random array of micropillars or a hexagonal array of micropillars. All the micropillars were assumed to be identical and characterized by the diameter $d = 10$ μm. Both samples were produced to have a surface coverage of about 10%, which for the hexagonal array, corresponds to the lattice constant $a = 30$ μm. The source used to illuminate these samples was light from a Xenon lamp, filtered at the center wavelength $\lambda = 535$ nm by a window of 10 nm spectral width, that was unpolarized. The subplots in Fig. 5 correspond to the polar angles of incidence $\theta_i = 10°$, 30°, and 60°, and in all cases, the azimuthal angle of incidence is $\phi_i = 180°$ (top to bottom in Fig. 5). As expected, the measured data show reflection symmetry with respect to the plane of incidence. Therefore, for reasons of convenience, we have combined the presentation of the results for the random and regular arrays for the same surface coverage. This is done in such a way that the upper halves of each of the subplots in Fig. 5 [$0° < \phi_t < 180°$] represent the normalized DTCs for the random arrays, while the lower halves [$180° < \phi_t < 360°$] present the corresponding results for the regular array. The various insets in Fig. 5 present the details in an angular region around the direction of specular transmission. The first striking observation to be made from the results presented in Fig. 5 is how similar the angular intensity distributions for the random and the regular arrays of micropillars are. Of course, the transmitted intensity distributions for the random array do not display diffractive orders, as is the case for the intensity distributions for the corresponding regular array. Hence, it is the intensity envelopes of the latter data sets that are similar to the corresponding intensity distributions obtained for the random array.

Before further discussing the several interesting features that can be observed in the measurements reported in Fig. 5, we present additional measurements obtained by the multimodal microscope in Fig. 6 for the same random array used in obtaining the results presented in Fig. 5. In particular, Fig. 6 shows results for polar angles of incidence $\theta_t = 0°$, 10°, 20°, and 30° and without any angular restriction in the collection arm of the microscope [i.e., $\theta_t \leq 45°$]. Again one finds that the intensity patterns measured with the microscope agree rather well with the corresponding results obtained with the goniospectrophotometer. It should be remarked that, located at the lower right edges of Figs. 6(a)–6(c), one can see a few irregular spots (in yellow). These features we believe to be due to contamination present on the surfaces of the optical elements of the microscope, and they are visible only when the intensity measurement requires an extremely high dynamic range. These irregular features are therefore artifacts and must not be considered as part of the light scattered by the sample.

The results presented in Figs. 5 and 6 show explicitly that halos are present in the angular distribution of the transmitted intensities for *both* regular and random arrays of micropillars if $\theta_i \neq 0°$. Furthermore, for both array types, we find that the polar angle of transmission defining the halo is related to the polar angle of incidence by the relation $\theta_t = \theta_i$, which for our geometry, also is the polar angle of the specular direction of transmission. These results suggest that the presence of the halo is related to individual micropillars and their cylindrical shape rather than to how they are arranged on the surface of the substrate.

The origin of the halo can in fact be understood within the framework of either the extended Mie theory for non-spherical particles [6] or the Debye series approach [19]. According to the latter formalism, the origin of the halo can be attributed to rays that have been directly transmitted through the micro-sized cylinders (as in an optical fiber), or that have been directly

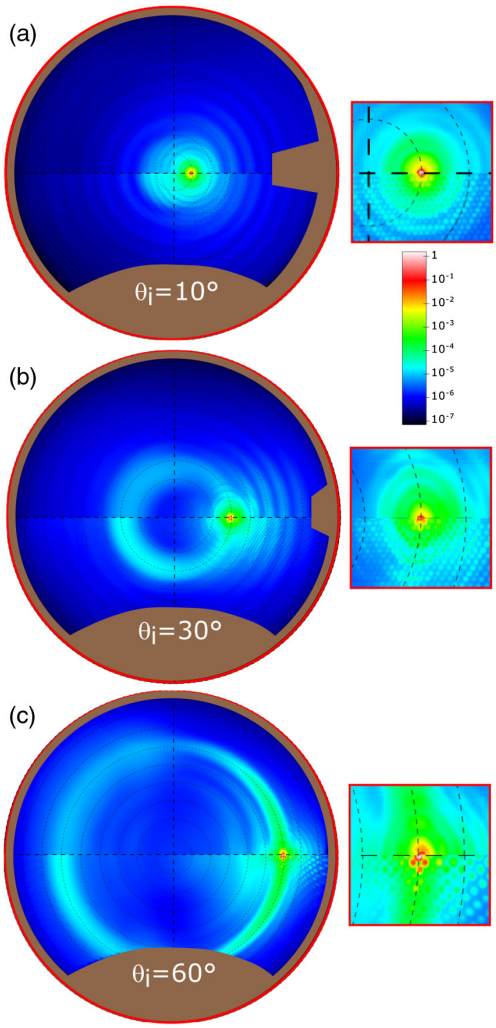

Fig. 5. Angular dependence of the DTCs for the polar angles of incidence (a) $\theta_i = 10°$, (b) 30°, and (c) 60° measured with the goniospectrophotometer and normalized by their maximum values (found in the specular direction). The insets zoom in on ±15° angular regions around the specular directions. The samples consist of a random array of micropillars (upper halves) or a hexagonal regular array of micropillars (lower halves). All micropillars are characterized by a diameter and a height of $d = 10$ μm and $h = 10$ μm, respectively. The surface coverage of the two arrays is approximately 10%, which for the regular array, corresponds to the lattice constant of $a = 30$ μm. In the case of the regular array, one aims for the plane of incidence to be aligned with one of the lattice vectors $\mathbf{a}_i$ ($i = 1, 2$). The source of the incident light is a Xenon lamp filtered around the center wavelength $\lambda = 535$ nm by a window of width 10 nm. The dashed grid circles are separated by a polar angle of 10°.

reflected (or scattered) by the outer surface of the cylinders. A detailed analysis of the halo and its origin will be presented in a separate publication using polarization-dependent measurements and numerical simulations. This study will be based on polarization-sensitive measurements, and it concludes that the halo is a consequence of reflection and/or transmission of light by *individual* cylinders, and not due to, for instance, multiple reflections or the excitation of leaky guided modes in the glass slide (substrate).

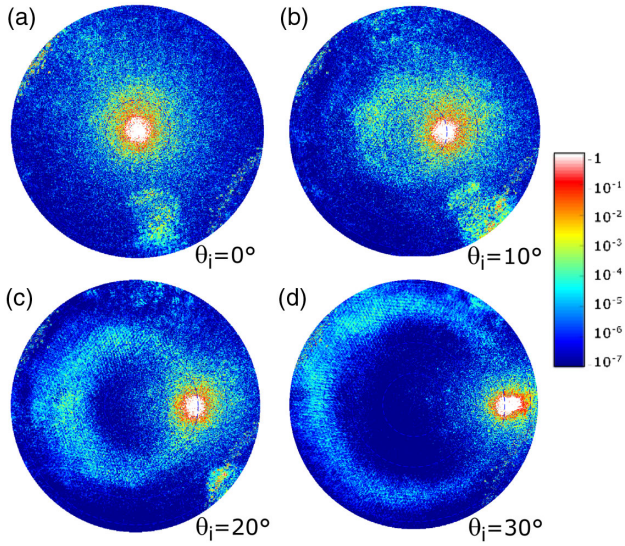

Fig. 6. Far-field distribution of the normalized total intensity transmitted through a glass substrate patterned with a random array of micropillars of a surface coverage of 10%. The measurements were performed by the multimodal microscope in Fourier imaging mode. The polar angle of incidence of the illuminating beam is assumed to be (a) $\theta_i = 0°$, (b) 10°, (c) 20°, and (d) 30°. The angular aperture of the illumination beam is set to 10° in all cases, and the measurements were performed for the wavelength $\lambda = 533$ nm.

3. Concentric Circular Fringes

During the discussion of the results presented in Figs. 3(a)–3(b), we observed two classes of concentric circular intensity patterns: *class 1 fringes* are concentric about the direction defined by $\theta_t = 0°$, while *class 2 fringes* are centered around the direction of specular transmission $(\theta_t, \phi_t) = (\theta_i, 0°)$. The azimuthally symmetric circular fringes that are centered at $\theta_t = 0°$ are readily observed in Fig. 7(a) for sufficiently large values of θ_t; these are the class 1 fringes for this configuration. In particular, what is presented in Fig. 7(a) are the angle-resolved DTCs for normal incidence obtained for two square arrays of micropillars, where the micropillars of the first have diameter $d = 40$ μm (upper half) and the second $d = 20$ μm (lower half). The lattice constants are rather different for the two arrays and defined by $a = 2d$. In both cases, the heights of the micropillars are $h = 10$ μm. The surface coverage of square lattices is given by $\rho = (\pi/4)(d/a)^2$, and hence the two square arrays have the same surface coverage [$\rho = \pi/16$]. A comparison of the results in the upper and lower halves of Fig. 7(a) reveals that the (class 1) fringes for the two samples are rather similar, even if the size of the micropillars and the lattice constants are different for the two samples. However, a careful inspection of the results presented in the lower half of Fig. 7(a) shows fringes that are not fully concentric about $\theta_t = 0°$. Furthermore, when the illumination is oblique, the azimuthal symmetry of these fringes is lost, as seen in Fig. 5, for instance, but the fringes remain centered at $\theta_t = 0°$. It should be noted that class 1 fringes are also present in the intensity of the light transmitted through random arrays of micropillars [Fig. 5; upper halves].

These results seem to rule out a specific size or organization of the micropillars as the explanation of the (class 1) fringes.

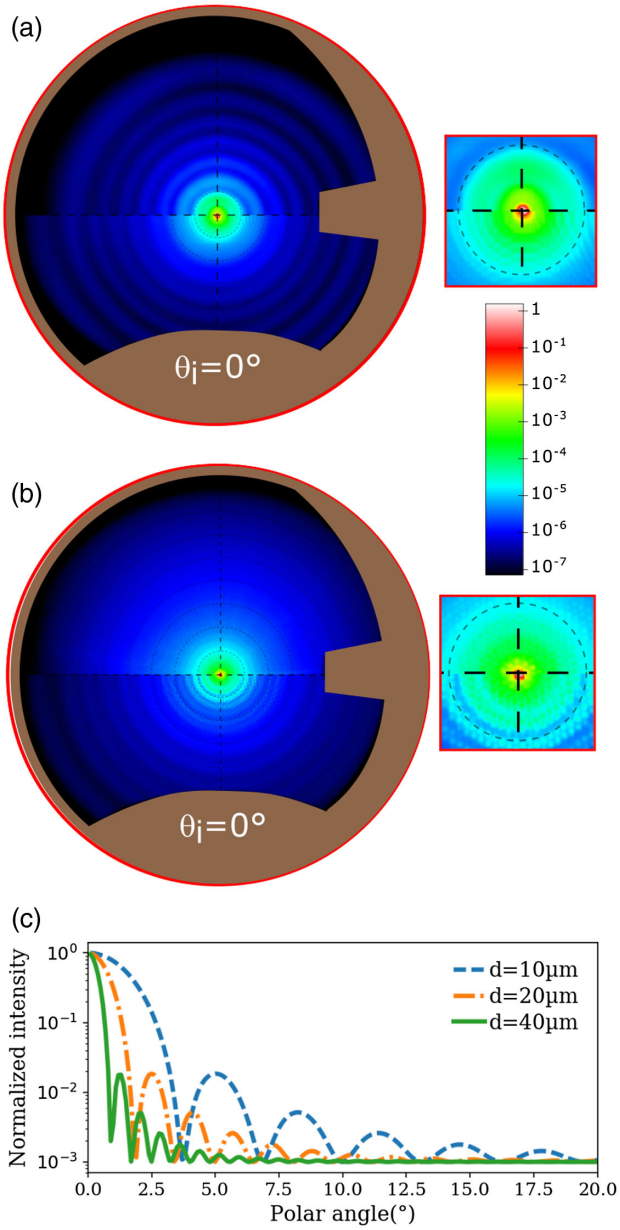

Fig. 7. Angle-resolved DTCs for (a) square or (b) hexagonal arrays of supported micropillars obtained at normal incidence [$\theta_i = 0°$]. The illumination was done with a Xenon lamp filtered at the center wavelength $\lambda = 535$ nm by a window of width 10 nm. (a) The diameters of the micropillars and the lattice constants of the square arrays were, respectively, $d = 40$ μm and $a = 80$ μm (upper half); and $d = 20$ μm and $a = 40$ μm (lower half). (b) A hexagonal array of micropillars defined by $d = 10$ μm and $a = 30$ μm measured with (upper half) and without (lower half) a black cover on both the front and the back side of the sample. Each cover has a 3 cm hole in diameter that is big enough not to interact with the incident beam, and is aligned with the incident beam. (c) Airy patterns from Eq. (3) for circular apertures of diameter 10 μm, 20 μm, and 40 μm, respectively.

To better understand their origin, we conducted an additional experiment on the sample used to produce the results in Figs. 3(a)–3(b) [hexagonal array of micropillars defined by $d = 10$ μm and $a = 30$ μm]. Now the sample was covered by black paper on the front and back surfaces, which had holes of 3 cm diameter that were aligned with the normally incident beam. The diameter of the holes was chosen to be larger than the full width of the incident beam in order to allow the transmission of the direct beam, but at the same time, partially block some of the light that presumably is partially guided inside the sample. A comparison of the angular distribution of the DTCs with or without the black covers is presented in Fig. 7(b) as the upper half and lower halves, respectively. These two data sets show clearly that the class 1 fringes vanish, or at least are significantly suppressed, when the sample has black front and back covers.

A careful study of the results in Fig. 5 reveals that for a given polar angle of incidence, the class 1 fringes for the random array (upper halves) and the periodic array (lower halves) appear at different polar angles of transmission; in particular, this is apparent in Fig. 5(b). However, other periodic samples show class 1 fringes whose angular positions are more similar to the results for the random pattern presented in Fig. 5. The difference in angular positions of the class 1 fringes observed in Fig. 5 we suspect is not a result of how the pillars are organized, but rather a consequence of a slight difference in pillar height between the random and periodic samples. In particular, we speculate that the class 1 fringes are related to Selényi rings [20], whose angular positions are known to depend on the film thickness (pillar height). Such rings are interference fringes whose angular positions are indeed independent of the polar angle of incidence and are centered around the direction $\theta_t = 0°$ in the case of transmission. Following an analysis similar to that in Ref. [20] [see Eq. (36)], we predict the polar angular positions of the Selényi rings to be $\theta_t = \theta_t^\star$, where $\theta_t^\star$, for instance, can be 69.4°, 60.0°, 51.7°, 43.7°, 35.2°, or 25.2° (leaving out some of the lower/higher values not relevant for this discussion).

These angles were calculated assuming a wavelength $\lambda = 535$ nm; the experimental measured dielectric constant of glass at this wavelength $\varepsilon = 2.23$; and finally a pillar height of $d = 10$ μm. It is found that these predicted values of $\theta_t^\star$ compare favorably to those that can be observed for the DTCs of random arrays in Fig. 5 [upper halves]. Calculations for 10.5 μm reveal the shift in fringes similar to that observed in Fig. 5(b). However, further research is needed to clarify these issues, and to establish whether the class 1 fringes that we observe are indeed Selényi interference rings for both random and regular arrays.

Additional fringes, which are of a type other than those we just discussed, are observed in the intensity transmitted through regular or random arrays of micropillars that are concentric about the direction of specular transmission. For instance, in the insets in Figs. 5(a) and 7(a), showing the details around the specular direction of transmission, they are seen for smaller values of $\theta_t - \theta_i$ (and $\phi_t - \phi_i - 180°$), and these fringes are examples of the class 2 fringes. Note that such fringes are also seen in Fig. 3(b). The class 2 fringes are in the measured data superimposed on the class 1 fringes, so that it can be challenging to distinguish them in certain cases. However, the "frequency" of the class 2 fringes is typically found to be significantly higher than the "frequency" of the class 1 fringes. The class 2 fringes do depend on the size of the micropillars, which contrasts with what we found for the class 1 fringes. For instance, the upper and lower halves of Fig. 7(a) compare DTCs for regular arrays of micropillars of different sizes (and lattice constants); the

diameters of the micropillars are $d = 20\ \mu\text{m}$ and $d = 40\ \mu\text{m}$, respectively. From the inset in this figure, it is found that the polar angle separation between consecutive fringes close to the specular direction is smallest for the array consisting of micropillars of the largest diameter. Furthermore, the class 2 fringes, like their class 1 counterparts, can be observed for both regular and random arrays of micropillars. In Fig. 5(b), the class 2 fringes are observed clearly as oscillations along the halo for both the random and regular arrays, and the angular distance between them is of the same order for both cases. These results we take as indications that the class 2 fringes are related to the size of the micropillars, not to how they are organized along the surface of the substrate.

The results for the class 2 fringes for normal incidence presented in Figs. 7(a)–7(b) we rationalize in the following way. The normally incident light of wavelength λ is assumed to couple into the micropillars of diameter $d \sim 10^1\lambda$. This guided light will be radiated into the glass slide by the open-ended circular waveguide giving rise to an Airy-like diffraction pattern predicted by Fraunhofer diffraction [5]. Taking a circular aperture, for simplicity, the expression for the normalized transmitted intensity distribution of the diffracted light reads [5]

$$\bar{I}(\theta_t) = \left(\frac{2\mathrm{J}_1\left(\pi \frac{d}{\lambda} \sin\theta_t\right)}{\pi \frac{d}{\lambda} \sin\theta_t} \right)^2, \tag{3}$$

where J_1 denotes the Bessel function of the first kind and order one, and d denotes the diameter of the aperture that we will set equal to the diameter of the micropillars [5]. Such normalized intensity distributions are shown in Fig. 7(c) for diameter $d = 10\ \mu\text{m}$, 20 μm, and 40 μm, respectively. The "frequency" of the oscillations observed in the transmitted intensities in the region around the specular direction of transmission is clearly different for the two samples considered in Fig. 7(a), and the trend that one finds is in agreement with the prediction of Eq. (3) [see also Fig. 7(c)]. This demonstrates the high sensitivity of the angular position and intensity of the oscillations to the diameter of the cylinders, which is in good agreement with the predictions made on the basis of the Fraunhofer diffraction formalism. A direct comparison of the measurements and the Airy patterns is not straightforward for samples with a regular array of pillars, since the Airy pattern is modulated by the presence of diffraction orders.

B. Haze and Gloss

Two of the most commonly used integral optical measurements are haze and gloss. According to the two standards, ISO 14782:1999 [21] and ASTM D1003-13 [22], haze is defined as the percentage of transmitted intensity passing through a specimen that deviates from the specular direction of transmission by more than 0.044 rad (2.5°) [23]. Similarly, gloss is defined as the total intensity scattered inside a small angular region about the specular direction normalized by the intensity that is scattered by a standard sample; this ratio defines the "gloss unit" scale. According to the standards ISO 2813:2014 [24] and ASTM D523-14 [25], gloss can be measured at three different polar angles of incidence: $\theta_i = 20°$, 60°, and 80° [26].

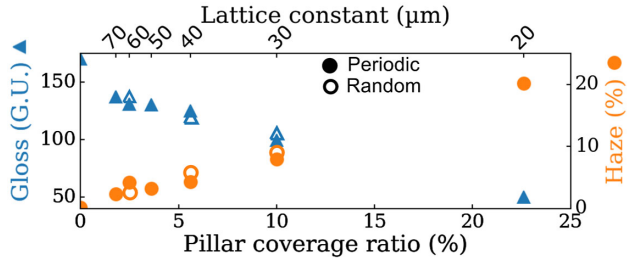

Fig. 8. Measured haze and gloss values for hexagonal arrays of micropillars (filled symbols) or random arrays of micropillars (open symbols). The gloss values were measured with the glossmeter (Enrichsen—Pico Glossemaster Model 500) in reflection at $\theta_i = 20°$. The haze values were obtained by a hazemeter (BYK Gardner Hazegard plus) in transmission at $\theta_i = 0°$. The diameter and height of all micropillars are both 10 μm.

We will now discuss the haze and gloss values that can be obtained for our supported regular and random arrays of micropillars. The gloss measurements that we report were performed in reflection for a polar angle of incidence of $\theta_i = 20°$, while haze was measured in transmission for normal incidence [$\theta_i = 0°$]. Figure 8 presents the experimental values obtained for haze and gloss (filled symbols) as functions of the surface coverage of the supported arrays by the use a hazemeter and a glossmeter. These results were obtained by keeping the diameter of the pillars constant at $d = 10\ \mu\text{m}$ and changing the lattice constant of the hexagonal array between $a = 20\ \mu\text{m}$ and 80 μm. We also performed measurements of haze and gloss for some samples of random arrays of micropillars [open symbols in Fig. 8], and only minor differences were found between values of these quantities obtained for regular and random arrays of the same surface coverage. From the results presented in Fig. 8, it is observed that the overall trend is that haze (in transmission) is an increasing (and approximately linear) function of the surface coverage, while gloss decreases as a function of the same quantity. The increase in haze with surface coverage indicates an increase in the amount of light transmitted away from the specular direction by more than 2.5°. This observation is consistent with the decreasing level of measured gloss for the same samples. It is tempting to interpret this observation as a decrease in the specular component of the transmitted intensity with increasing surface coverage, while at the same time, the diffuse component increases.

When the angular dependency of the DTC is integrated over the full solid angle of transmission [$d\Omega_t = \sin\theta_t d\theta_t d\phi_t$], the transmittance of the sample is obtained [17]. To calculate the haze of a sample from the angular distribution of the DTC measured for a given angle of incidence, one proceeds in the following way. First, one performs a solid angle integration of the DTC over an angular region around the specular direction of transmission $(\theta_t, \phi_t) = (\theta_i, \phi_i - 180°)$ defined by $|\theta_t - \theta_i| \leq \Delta\theta_t$. For given angles of incidence, the haze of the sample is calculated by first dividing the result obtained in this way by the transmittance and then subtracting the resulting ratio from unity (see Ref. [23]). We have chosen $\Delta\theta_t = 2.5°$ to be consistent with the standard, and what is assumed in the construction of the hazemeter.

Figure 9 compares the haze values calculated in this way from the angle-resolved DTC measurements with the values obtained by direct haze measurements performed on the same samples of hexagonal arrays in transmission and at normal incidence; in such calculations, the missing data points were set to zero. One finds good agreement between haze values measured directly and values calculated from the measured angle-resolved DTC data. This testifies to the consistency of the angle-resolved measurements and their normalization. For instance, the haze values calculated from the angle-resolved DTC data are 18% for lattice constant $a = 20$ μm (or surface coverage $\rho = 23\%$); 9% for $a = 30$ μm [$\rho = 10\%$]; and 2% for $a = 60$ μm [$\rho = 3\%$]. These values should be compared to the corresponding measured haze values for the same samples, which are 20%, 8%, and 4%, respectively. An increase in the lattice constant a, or equivalently, a decrease in the surface coverage ρ, causes more of the diffractive orders to end up inside a cone of angular width $\Delta\theta_t$ about the specular direction, and hence, the value of haze to drop. Yet, transmission efficiencies of individual diffraction orders are naively expected to decay with increasing lattice constant and increasing order. Therefore, for a sufficiently large lattice constant, a further increase in it will only marginally affect the resulting haze value. However, for smaller lattice constants, for which only a few diffractive orders fall inside $\Delta\theta_t < 2.5°$, this is no longer the case. Thus, based on haze values measured with a hazemeter alone, we are not able to distinguish a regular array from a random array if the surface coverage is sufficiently large. For reasons of comparison, Fig. 9 also reports results for the calculations assuming $\Delta\theta_t = 1°$, a value suggested as more realistic in a recent study on the angular width of specular beams [27]. As expected, when using this value for $\Delta\theta_t$, the calculation procedure results are higher than the haze values for the same sample. However, the interesting observation is not that one gets larger values, but how much larger the obtained values are. For small values of the surface coverage, or larger lattice constants, the difference between the results obtained when using these two values for $\Delta\theta_t$ in the calculation of haze is not very dramatic. However, for the larger values of the surface coverage, the differences increase.

When the visual aspect of an object is to be taken into account, the particularities of the human eye, rather than those of an artificial detector, must be considered. For instance, the angular resolution of the human eye is about 0.03° [28]. If haze is intended to quantify the fraction of transmitted intensity that is transmitted away from the specular direction (of transmission), the use of the value $\Delta\theta_t = 2.5°$, which is perfect for a number of industrial needs, is far too large when it comes to discussing human visual perception of the optical response of 1D or 2D gratings.

For the sake of illustration, let us restrict ourselves to a 1D grating at normal incidence for which the polar angle of the propagating diffractive orders in transmission is given by $\sin\theta_m = m(\lambda/a)$, with m an integer ($m \in \mathbb{Z}$) and $m = 0$ corresponding to specular transmission. For this system, the number of propagating diffracted orders in transmission is (red curve in Fig. 10) $N = 2\lfloor \frac{a}{\lambda} \rfloor + 1$, where $\lfloor x \rfloor$ denotes the floor function of x, which returns the greatest integer less than or equal to its argument x. Patterns with lattice constants $a < \lambda$ exhibit a single (fundamental) diffractive order $m = 0$, which corresponds to specular transmission. But in the case of $a \geq \lambda$, at least two additional diffractive orders are present. At normal incidence, the two first diffractive orders [$m = \pm 1$] are symmetric about the specular direction and correspond to the polar angles of transmissions $\pm\theta_1$. Figure 10 illustrates the variation of the angle of the first diffracted order θ_1 under the assumption of normal incidence [$\theta_i = 0°$]. The green solid line in this figure corresponds to an illumination wavelength of $\lambda = 500$ nm, while the green area around this line represents the variation due to the whole visible range of wavelengths from 380 to 780 nm. Moreover, the red solid curve in Fig. 10 illustrates the total number of diffraction orders in such a system.

For a lattice constant of about $a = 9$ μm and an illuminating wavelength of $\lambda = 380$ nm, the first diffracted order will

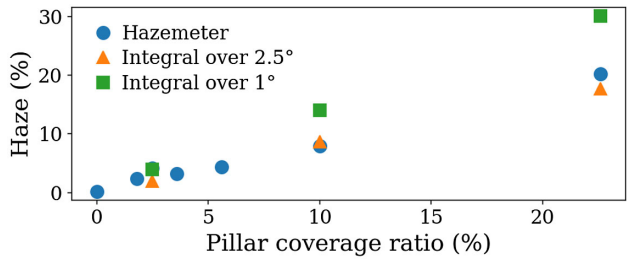

Fig. 9. Comparison of the haze values for hexagonal arrays obtained with the hazemeter (direct measurements) and those calculated from angular resolved DTC data as functions of the surface coverage. The DTC data used in obtaining these results were measured at normal incidence by the use of the goniospectrophotometer. The measurement configuration was identical (accept for the angles of incidence) to what was used in obtaining the results in Fig. 3(a). The way that haze was calculated from such data is described in the main text. The value of the polar angular interval $\Delta\theta_t$ assumed in such calculations is given in the legend. It is noted that the value $\Delta\theta_t = 2.5°$ corresponds to the norm of haze measurements. The diameter and height of all micropillars are both 10 μm.

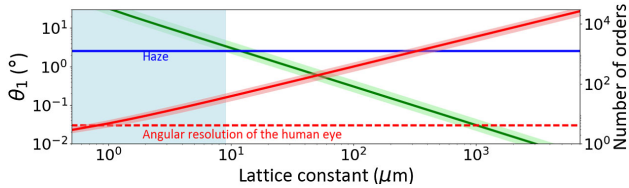

Fig. 10. Normally incident light [$\theta_i = 0°$] diffracted through a surface consisting of a one-dimensional grating of lattice constant a. The green line shows the angle of diffraction θ_1 of the first diffraction order [$m = 1$], while the red line represents the total number of propagating diffracted orders N, both obtained by assuming the wavelength $\lambda = 500$ nm for the incident light. The corresponding green and red shaded areas (around the solid lines of the same color) represent the variations of these two quantities due to the wavelength of the incident light varying over the visible range of 380–780 nm. The blue horizontal line corresponds to the smallest diffraction angle [2.5°] for which the diffracted light in transmission contributes to haze. Haze measurements for lattice constants smaller than approximately 9 μm receive contribution from all higher-order diffractive orders for which $m \neq 0$. However, for larger lattice constants, not all such higher orders will contribute. For comparison, the horizontal red dashed line corresponds to the limit of angular resolution of the human eye.

enter into the "specular" area of the haze measurement. Starting from this wavelength (and higher) the haze measurements, as a measure of the fraction of transmitted intensity away from the specular direction, are biased (unshaded region of Fig. 10). For lattice constants all the way up to $a = 1$ mm, a human observer will be able to distinguish specular transmission from the first diffraction order. These results hint towards a not optimal definition of haze for gratings of long periods compared to the wavelength of visible light. According to our discussion, when the visual aspect of gratings with large periods matters, a haze definition making use of smaller angular spread around the specular direction than the actual 2.5° defined in the norms would provide objective haze values that would be in agreement with the subjective experience of the human eye.

4. CONCLUSION

We report angle-resolved transmitted intensity measurements for a set of regular or random arrays of dielectric micropillars [diameter: 10 μm to 40 μm; height:10 μm] in the low-coverage limit that are supported by thin index-matched glass slides. The regular arrays were characterized by lattice constants in the range of $a = 20$ μm to 80 μm. Yet, the analysis we provide in this paper is not limited to micropillar geometry but applies equally well to patterns with sub-millimeter features of unit cell elements and sub-millimeter periodicity, which are larger compared to conventional gratings for visible light applications. The measurements were performed by a goniospectrophotometer at wavelength $\lambda = 535$ nm but also by a multimodal imaging polarimetric microscope, and the two sets of measurements gave comparable results. On the basis of the experimental data obtained in this way, it is demonstrated that all examined regular arrays exhibit diffraction orders of non-negligible intensity. Moreover, for identical micropillars, the mean differential transmission coefficients for the random arrays agree well with the envelope of the same quantity for the regular array under the assumption that the surface coverage is the same. Furthermore, the angle-resolved measurements display unique diffractive (halo and fringes) features that are due to properties of single micropillars and not to how they are organized along the surface. In further work, a detailed numerical analysis of the halo will be provided, together with a study of its sensitivity to the system geometry. Finally, we perform a comparison of direct measurements of haze in transmission for our structured samples with what can be calculated from the angle-resolved transmitted intensity measurements. Good agreement between the two types of results is found, which testifies to the accuracy of the angle-resolved measurements that we report. However, we find that for larger surface coverage, haze values alone cannot be used to distinguish regular and random arrays of micropillars. These correspond to cases when angular separation between diffraction orders is distinguishable by a human eye even under broadband illumination.

Funding. French National Research Agency (ANR-15-CHIN-0003, IDEX Paris-Saclay ANR-11-IDEX-0003-02).

Acknowledgment. We thank Gael Obein, Guillaume Ged, Sebastien Noygues, Emmanuel Garre, and Jean-Philippe Banon for valuable discussions.

REFERENCES

1. T. Candela, F. Renard, Y. Klinger, K. Mair, J. Schmittbuhl, and E. E. Brodsky, "Roughness of fault surfaces over nine decades of length scales," J. Geophys. Res. **117**, B08409 (2012).
2. B. Bhushan, "Biomimetics: lessons from nature-an overview," Phil. Trans. R. Soc. A **367**, 1445–1486 (2009).
3. J. C. Stover, *Optical Scattering: Measurement and Analysis*, 3rd ed. (SPIE, 2012).
4. I. Simonsen, "Optics of surface disordered systems: a random walk through rough surface scattering phenomena," Eur. Phys. J. Spec. Top. **181**, 1–103 (2010).
5. M. Born and E. Wolf, *Principles of Optics*, 7th ed. (Cambridge University, 2012).
6. A. Cohen and C. Acquista, "Light scattering by tilted cylinders: properties of partial wave coefficients," J. Opt. Soc. Am. **72**, 531–534 (1982).
7. E. G. Loewen and E. Popov, *Diffraction Gratings and Applications* (CRC Press, 1997).
8. J. D. Joannopoulos, S. G. Johnson, J. N. Winn, and R. D. Meade, *Photonic Crystals: Molding the Flow of Light*, 2nd ed. (Princeton University, 2008).
9. V.-C. Su, C. H. Chu, G. Sun, and D. P. Tsai, "Advances in optical metasurfaces: fabrication and applications [Invited]," Opt. Express **26**, 13148–13182 (2018).
10. J. Bico, C. Marzolin, and D. Quere, "Pearl drops," Europhys. Lett. **47**, 220–226 (1999).
11. B. He, N. A. Patankar, and J. Lee, "Multiple equilibrium droplet shapes and design criterion for rough hydrophobic surfaces," Langmuir **19**, 4999–5003 (2003).
12. A. L. Dubov, K. Perez-Toralla, A. Letailleur, E. Barthel, and J. Teisseire, "Superhydrophobic silica surfaces: fabrication and stability," J. Micromech. Microeng. **23**, 125013 (2013).
13. C. Turbil, I. Gozhyk, J. Teisseire, I. Simonsen, G. Ged, and G. Obein, "Predicting changes in visual appearance of periodic surface from BRDF measurements," arXiv:1703.00704 [cond-mat.mtrl-sci] (2017).
14. B. Brudieu, A. Le Bris, J. Teisseire, F. Guillemot, G. Dantelle, S. Misra, P. Roca i Cabarrocas, F. Sorin, and T. Gacoin, "Sol-gel route toward efficient and robust distributed Bragg reflectors for light management applications," Adv. Opt. Mater. **2**, 1105–1112 (2014).
15. S. H. Yoo, R. Ossikovski, and E. Garcia-Caurel, "Experimental study of thickness dependence of polarization and depolarization properties of anisotropic turbid media using Mueller matrix polarimetry and differential decomposition," Appl. Surf. Sci. **421**, 870–877 (2017).
16. F. O. Bartell, E. L. Dereniak, and W. L. Wolfe, "The theory and measurement of bidirectional reflectance distribution function (BRDF) and bidirectional transmittance distribution function (BTDF)," Proc. SPIE **257**, 154–160 (1981).
17. Ø. S. Hetland, A. A. Maradudin, T. Nordam, P. A. Letnes, and I. Simonsen, "Numerical studies of the transmission of light through a two-dimensional randomly rough interface," Phys. Rev. A **95**, 043808 (2017).
18. J. A. Kurvits, M. Jiang, and R. Zia, "Comparative analysis of imaging configurations and objectives for Fourier microscopy," J. Opt. Soc. Am. A **32**, 2082–2092 (2015).
19. F. Xu, J. A. Lock, and C. Tropea, "Debye series for light scattering by a spheroid," J. Opt. Soc. Am. A. **27**, 671–686 (2010).
20. J.-P. Banon, Ø. S. Hetland, and I. Simonsen, "Selective enhancement of Selényi rings induced by the cross-correlation between the interfaces of a two-dimensional randomly rough dielectric film," Ann. Phys. **389**, 352–382 (2018).
21. "Plastics– Determination of Haze for Transparent Materials," ISO 14782:1999.
22. ASTM D1003-13, *Standard Test Method for Haze and Luminous Transmittance of Transparent Plastics* (ASTM International, 2013).

23. I. Simonsen, Å. Larsen, E. Andreassen, E. Ommundsen, and K. Nord-Varhaug, "Haze of surface random systems: an approximate analytic approach," Phys. Rev. A **79**, 063813 (2009).
24. "Paints and varnishes– Determination of gloss value at 20 degrees, 60 degrees and 85 degrees," ISO 2813:2014.
25. ASTM D523-14(2018), *Standard Test Method for Specular Gloss* (ASTM International, 2018).
26. I. Simonsen, Å. Larsen, E. Andreassen, E. Ommundsen, and K. Nord-Varhaug, "Estimation of gloss from rough surface parameters," Phys. Status Solidi B **242**, 2995–3000 (2005).
27. F. B. Leloup, J. Audenaert, G. Obein, G. Ged, and P. Hanselaer, "Repeatability and reproducibility of specular gloss meters in theory and practice," J. Coat. Technol. Res. **13**, 941–951 (2016).
28. F. Zettler and R. Weiler, *Neural Principles in Vision* (Springer-Verlag, 1976), pp. 354–370.